

Article

Design Method of Core-Separated Assembled Buckling Restrained Braces Confined by Two Lightweight Concrete-Infilled Tubes

Boli Zhu *, Junyuan Zhao  and Yuqing Yang 

School of Civil and Resource Engineering, University of Science and Technology Beijing, Beijing 100084, China

* Correspondence: zboldy@ustb.edu.cn

Abstract: This paper introduces a novel type of buckling restrained braces (BRBs) called core-separated assembled BRBs (CSA-BRBs). These braces are comprised of two single BRBs that are confined by lightweight concrete-infilled tubes, which are longitudinally connected by two continuous webs. The CSA-BRBs utilize materials more efficiently by increasing the height of the webs to create a large inner cavity, leading to an economical design. This paper predicts the threshold of the restraint ratio of CSA-BRBs approximately. This is achieved by assuming that the maximum moment resulting from applied loads at mid-height is less than the moment-bearing resistance that is conducted according to the outermost fiber of the external restraining section reading yielding. Elastic-plastic numerical analysis is conducted using FEM with beam elements for CSA-BRBs that are subjected to both monotonic and cyclic axial loads. The load resistance, hysteretic performance, and failure mechanism of CSA-BRBs are investigated by varying their restraining ratios. It is recommended that the restraint ratio threshold of CSA-BRBs under monotonic axial compression is used as a bearing type and the restraint ratio threshold of CSA-BRBs under axially compressive-tensile cyclic loads as an energy-dissipation type. This method provides a complete design for CSA-BRBs.

Keywords: core-separated assembled BRB; elastic buckling load; load resistance; hysteretic response; restraint ratio threshold



Citation: Zhu, B.; Zhao, J.; Yang, Y. Design Method of Core-Separated Assembled Buckling Restrained Braces Confined by Two Lightweight Concrete-Infilled Tubes. *Appl. Sci.* **2023**, *13*, 4306. <https://doi.org/10.3390/app13074306>

Academic Editor: Amir M. Yousefi

Received: 27 February 2023

Revised: 17 March 2023

Accepted: 27 March 2023

Published: 28 March 2023



Copyright: © 2023 by the authors. Licensee MDPI, Basel, Switzerland. This article is an open access article distributed under the terms and conditions of the Creative Commons Attribution (CC BY) license (<https://creativecommons.org/licenses/by/4.0/>).

1. Introduction

Buckling restrained braces (BRBs) are typically composed of core components and external restraining members [1,2]. The core component is directly subjected to axial loads and laterally restrained during compression buckling by the external restraining members. It is a principal bearing and energy-dissipating member. The core is often constructed of steel with a low yield point to meet ductility standards. The outer load for the external restraint system, which is not directly subjected to axial pressure, is the lateral extrusion dispersed load acting on the core part, a flexural component. The external restraining members increase the bearing capability of the core member by providing lateral restraint, preventing overall instability and resulting in a complete hysteresis curve and superior energy dissipation performance of the BRB. BRBs can provide stable lateral stiffness and bearing capacity subject to earthquakes and wind loads; under medium or large earthquakes, the core is the first to enter yielding, consuming the earthquake's energy input, reducing the energy input to the main structure from the earthquake, and playing the role of energy dissipation and earthquake reduction. In addition, the torsional vibration pattern may control the structure's design for systems with severe plane abnormalities. The frame's stiffness can be increased in this case by modifying the BRB to meet the structure's initial vibration mode, which is a flat dynamic vibration mode, successfully reducing the system's torsion effect.

The existing BRBs are categorized into three categories based on their external restraining members: reinforced concrete restrained BRBs [3,4], steel and concrete restrained

BRBs [5], and all-steel restrained BRBs [6,7]. At present, the reinforced concrete restrained BRB is rarely used in the structural design, considering that reinforced concrete is easy to crack and the restraint effect is poor. The design methods of the steel and concrete restrained BRB and all-steel restrained BRB are relatively mature, and these BRBs are widely used in structural design. Zhao et al. [8] proposed a novel type of angle steel buckling-restrained brace (ABRB) and investigated its elastic buckling load, load resistance, and hysteretic performance numerically and experimentally. Hoveidae et al. [9] proved the short-core all-steel BRB could effectively reduce the story drifts of the frames. Judd et al. [10] investigated the failure mode and hysteretic performance of the web-restrained BRB under cyclic load. Guo et al. [11–13] investigated the elastic buckling behavior, load resistance, and hysteretic performance of all-steel BRBs such as triple-truss-confined BRB (TTC-BRB), and shuttle-shaped BRB (SS-BRB), numerically and experimentally. Jia et al. [14] numerically investigated the failure modes and buckling behavior of all-steel fish-bone-shaped BRB (FB-BRB). Tong et al. [15] studied the buckling behavior and hysteretic performance of steel angles assembled BRBs. Other research like Qu et al. [16], Sun et al. [17], Wang et al. [18], and Jiang et al. [19], also investigated the hysteretic performance of all-steel BRBs. Recently, the core assembling of BRBs has been commonly fabricated.

However, the existing BRBs generally use a single core, and their bearing capacity is limited. Guo et al. [20,21] and Zhu et al. [22] presented and studied the elastic buckling load, load resistance, and hysteretic performance of all-steel core-separated BRB (CS-BRB) theoretically, numerically, and experimentally. However, the all-steel rectangular tube-constrained BRB chord is welded by four plates of steel to a very flat rectangular steel tube, which is difficult to manufacture. The test proves that its rectangular steel tube is prone to tear damage at the welding seam under the extrusion force of the in-line core. Huang et al. [23] proposed and studied an all-steel assembled double-cores BRB (DCBRB). However, the external restraining members of DCBRBs are connected by bolts, which are complex in structure and require high machining accuracy.

For these reasons, improvements need to be made to facilitate fabrication and avoid, as far as possible, the direct action of the kernel bending on the tube wall to prevent the weld from tearing. In order to address the issues mentioned above while also meeting the requirements of lightweight and high bearing efficiency of BRB, which is formed by connecting two steel tube BRB with infilled concrete [24], which not only has the advantages of double cores and larger inner cavities but also has a mature process for making steel tube restrained BRB filled with lightweight concrete. Meanwhile, since direct contact between the core and the flat rectangular tube wall is avoided, seam tearing damage, as previously described, will not occur.

This paper introduces the composition characteristics, node structure, and stress mechanism of the dual-kernel BRB. Then the formula for the restraint ratio threshold is deduced according to the edge yield criterion of the BRB's outer constraint section. Finally, the bearing capacity under axial compression load and hysteretic energy dissipation under cyclic axial load is analyzed using the CSA-BRB beam unit model. The influence of the change in the restraint ratio on the failure modes, load resistance, and hysteretic performance of CSA-BRB is analyzed.

2. Composition and Characteristics of CSA-BRB

The CSA-BRB, formed by two steel tubes restrained limbs connected by webs, has the role of each component, as shown in Figure 1. Lightweight concrete can be filled in steel tubes, and the core can flexibly adapt to various cross-section types, such as a flat plate or a cross-shaped welding section. As is well known, the external restraint member only bears the bending moment, not the axial force. When considering the filler concrete material, the lightweight concrete's contribution can be eliminated and just considered filling material. In this approach, the split steel tube's section can be increased, and the spacing between the two steel tubes can be flexibly set, both of which can improve the external restraining members' bending rigidity. At the same time, cold-formed thin-walled steel tubes can be

used for steel tube sections, which are easy to obtain in the market. Therefore, CSA-BRB is a core-separated BRB with higher carrying efficiency and more practicality.

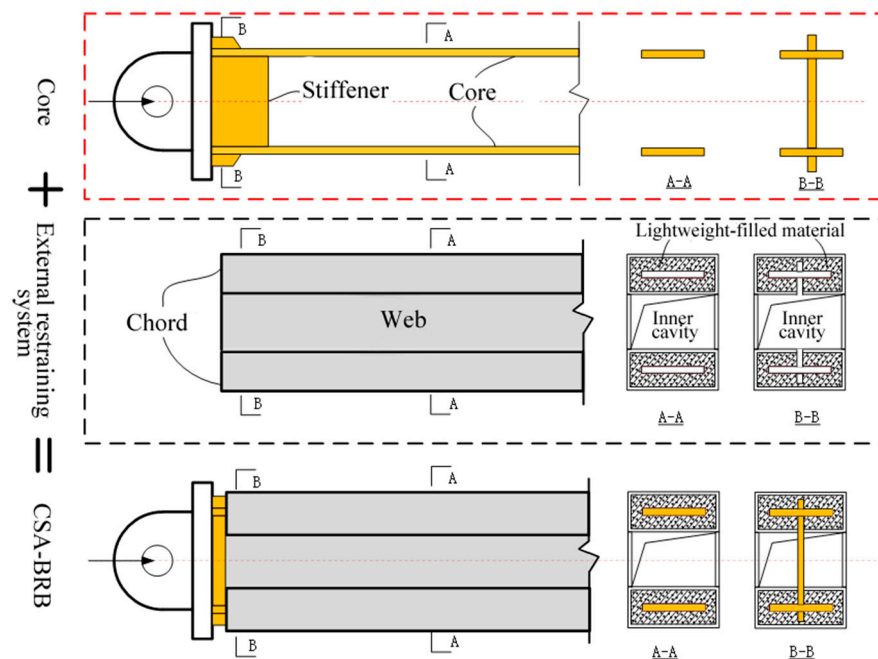


Figure 1. Composition of the proposed CSA-BRB.

When the ends of a core-separated BRB design are extended, the dual cores lose the constraint of the external components, and how their dual cores are effectively integrated to make a whole becomes a critical component of the core-separated BRB design. This section is outside the scope of this work; therefore, please refer to [22].

Obviously, by adjusting the gap between the CSA-BRB limbs, the inertia moment and bending stiffness of the external restraint section around the x -axis can be effectively increased. This paper focuses on the elastic buckling load, bearing capacity, and hysteretic energy dissipation performance of CSA-BRB hinged at both ends around the x -axis, corresponding to the design method around the y -axis, which is the same as that of a single solid web section BRB and is therefore not discussed further.

3. Calculation Method of the Restraint Ratio of CSA-BRB

The steel tube-constrained kernel split BRB restraint ratio is defined regarding the definition and design theory of the single-cored BRB restraint ratio. In order to ensure that the external restraining members of a steel tube restrained core separated BRB will not be unstable before the complete section of the core member yields, the restraint ratio ζ should be greater than a particular value, the restraint ratio threshold $[\zeta]$. A design that satisfies Equation (1) means that the overall instability of the CSA-BRB does not precede the yielding of the core.

$$\zeta = \frac{P_{cr,e}}{P_{y,c}} \geq [\zeta] \tag{1}$$

where $P_{cr,e}$ is the elastic buckling load corresponding to the restrained external member, excluding the contribution of the core, and $P_{y,c}$ is the initial yield load of the core.

To derive the elastic buckling load of CSA-BRB, it is simplified as a quasi-frame model shown in Figure 2, in which the middle column of the frame is facilitated by the external restraining members, including two steel tube chords and connecting two chords. The two cores are columns on both sides of the frame, connected by internal core ribs. In the structure, the lateral deflection deformation of the middle column and the columns on both

sides is the same. The axial displacement between the three is independent of each other. Elastic buckling loads for kernel-separated BRBs are derived from a quasi-frame model.

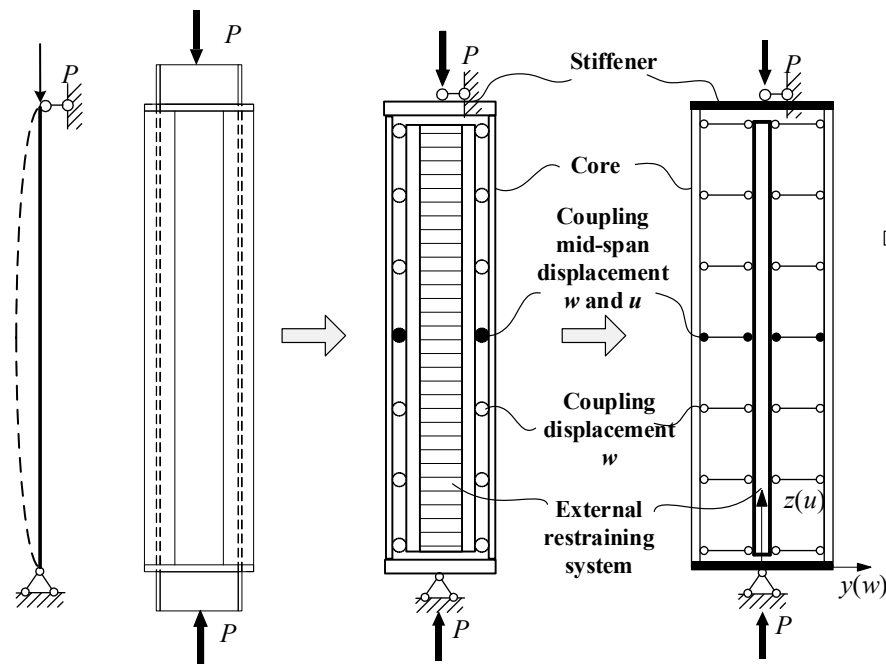


Figure 2. The simplified analytical and calculation model of a CSA-BRB.

Since the core’s moment of inertia around the x -axis is substantially smaller than the external restraining members’, the material’s elastic modulus rapidly decreases to zero after the core yields; the lateral stiffness of the core around the x -axis is minor compared to that of the external restraining members and can be ignored. Therefore, the elastic buckling load of the steel tube-restrained separated BRB external restraining members [20] is:

$$P_{cr,e} = \frac{(4+3.192\beta)}{(1+3.192\beta)} \frac{\pi^2 E_e I_e}{l^2}; \tag{2}$$

$$\beta = \frac{2(2E_{c1}I_{c1} + E_e I_e)}{E_{c1}A_{c1}h_e^2}$$

where the $E_e I_e$ is the lateral stiffness of the combined section around the y -axis of the external restraining members, calculated without taking into account the contribution of the filled lightweight material; $E_{c1}I_{c1}$ is the lateral stiffness of the core around the x -axis of its section, $E_{c1}A_{c1}$ is the compressive stiffness of the core, h_e is the axial distance between the two cores and l is the CSA-BRB length. The larger the β value, the stronger the combined effect of the two cores. Among them, the physical meaning β is the ratio of the sum of the bending stiffnesses of the two cores ($2E_{c1}I_{c1} + E_e I_e$) and the external restraining members to the bending stiffness calculated by the two cores according to the axis-shift theorem ($E_{c1}A_{c1}h_e^2/2$). The larger the value of β , the stronger the combined effect of the two cores.

According to the overall instability damage mechanism of the CSA-BRB, when the outermost fibers of the span section of the external restraining members reach their yield stress, the lateral stiffness of the span section of the external restraining members begins to decrease. With the continuous development of the yield zone of the external restraining members, the restraint stiffness of the restraint system is continuously reduced until the overall failure of the CSA-BRB occurs. Therefore, based on the edge-yielding criterion of the combined section of the external restraining members, the formula of its restraint ratio threshold is derived. According to the flexural bearing capacity M_u of the cross-section of

the external restraining members, it is not less than the bending moment M_e generated by the external load in the mid-span section, that is:

$$M_u \geq M_e \quad (3)$$

Similar to the BRB of the all-steel solid-web section, the flexural bearing capacity M_u of the cross-section of the CSA-BRB external restraining members is determined based on its edge yield criterion, which can be expressed as:

$$M_u = W_e f_{y,s} \quad (4)$$

where M_u is the sectional resistance moment of the external restraining members.

Borrowing from the expression for the bending moment in the span section of a single-cored BRB under axial load P , the bending moment M_e in the span is given for a CSA-BRB core with an axial compression strain of 0.02 and taking into account the effect of the initial defect (Equation (5)), where η is the strengthening factor considering the core material, α is the adjustment parameter determined when the restraint ratio threshold is determined later and v_0 is the initial defect of CSA-BRB, which is taken as $l/500$.

$$M_e = \frac{\alpha \eta P_{y,c} v_0}{1 - \eta P_{y,c} / P_{cr}} \quad (5)$$

Substituting Equations (4) and (5) into Equation (3) and introducing the restraint ratio $\zeta = P_{cr,e} / P_{y,c}$, the restraint ratio threshold $[\zeta]_\eta$ for a bearing CSA-BRB considering the strengthening factor of the core material under monotonic axial compression load is obtained in Equation (6), where $f_{y,s}$ is the yield strength of the steel in the externally restrained combined section.

$$[\zeta]_\eta = \frac{\eta W_e f_{y,s}}{W_e f_{y,s} - \eta \alpha P_{y,c} v_0} \quad (6)$$

Under the action of axial cyclic load, the steel tube restrained kernel separated BRB has to meet the energy dissipation requirement, the cumulative plastic deformation factor of the CSA-BRB under repeated load $\mu_c \geq 200$, so the restraint ratio threshold of the energy dissipating BRB should be more stringent than that of the bearing type. Referring to the American Code for Seismic Steel Construction AISC341-05 [25], considering the strain strengthening adjustment factor ω for the core steel, the steel tube restrained core separated BRB energy dissipative restraint ratio threshold $[\zeta]_\omega$ is calculated according to Equation (7).

$$[\zeta]_\omega = \frac{\omega W_e f_{y,s}}{W_e f_{y,s} - \omega \alpha P_{y,c} v_0} \quad (7)$$

4. CSA-BRB Ultimate Bearing Capacity Parasitic Bearing Restraint Ratio Threshold

4.1. Finite Element Model

In this section, the FE software ANSYS 14.5 is used to establish the finite element model (FEM) of CSA-BRB for elastoplastic static bearing capacity analysis, and the contribution of the infill material is ignored in the numerical analysis. Both core and restrained external members are simulated using beam unit BEAM188 to save computational costs and improve computational efficiency. The core member uses a one-piece plate, and the restrained external system uses a combined section and forms a custom beam unit, as shown in Figure 3.

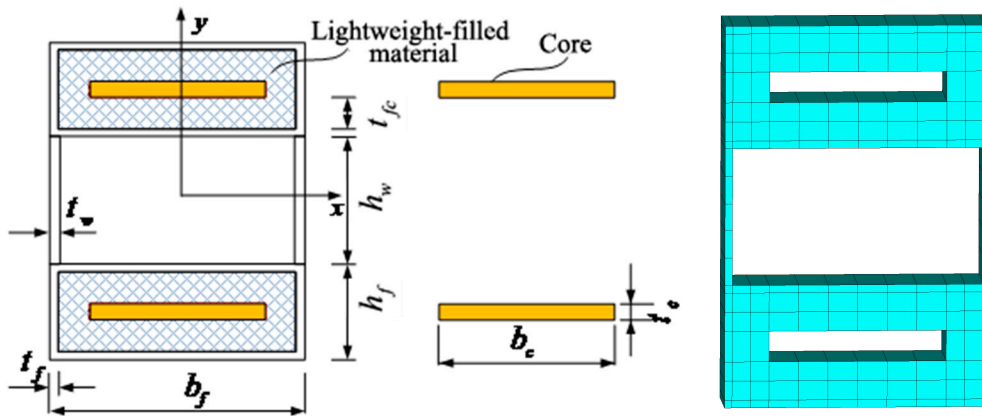


Figure 3. Section of the CSA-BRB.

The displacement couplings between the core and external restraining members are illustrated in Figure 4, where the lateral deformation of the core and external restraining members is coupled via point-to-point lateral deflection displacement; in the CSA-BRB mid-span, the axial displacement of the corresponding nodes of the core and external restraining members in the mid-span section is coupled to eliminate ribs at the end of the core are rigidly connected to the core. They are not coupled to the external restraining members.

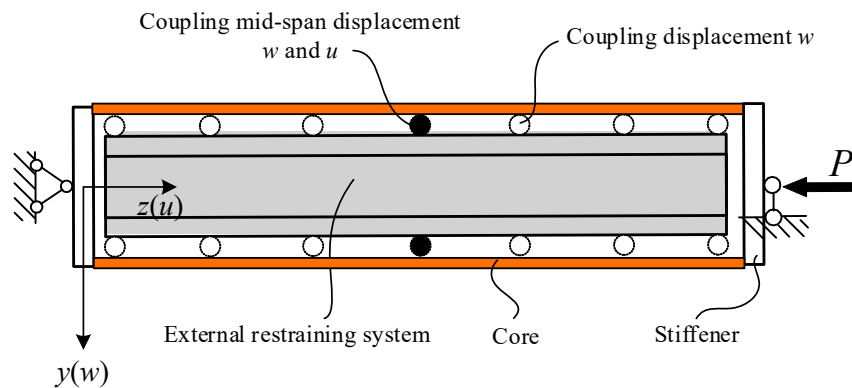


Figure 4. Lateral displacement coupling between the core and the restrained system.

As shown in Figure 4, the two ends of the CSA-BRB are hinged to constrain the x , y , z displacements of the span nodes of the ribs on one side of the core and the x , y displacements of the ribs on the other side; the overall lateral (x -direction) displacement of the CSA-BRB is also constrained to ensure that it bends around the x -axis; finally, the rotational displacement of the CSA-BRB around its axis (x -direction) is constrained to avoid rigid body rotation. Numerical analysis of elasticity and plasticity is carried out by applying an axial load P to the end of the CSA-BRB.

For the calculations designed in this section, the kernel is selected from a hot-rolled steel plate, using Q235 steel with a yield strength of $f_y = 235$ MPa. The rectangular steel tubes of the outer restraining members are cold-formed thin-walled rectangular tubes of Q355 steel with a yield strength of $f_y = 355$ MPa. The end stiffeners are set to be elastic, and the module of elasticity of the steel $E_s = 206$ GPa, Poisson's ratio $\nu = 0.3$. The material properties of the steel of the external restraining members are taken as ideal elastoplasticity; the σ - ϵ curve of the core is shown in Figure 5. The steel obeys the follower strengthening criterion during the elastoplastic analysis.

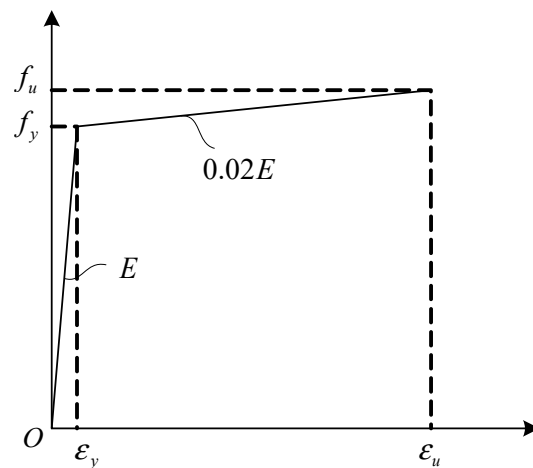


Figure 5. The σ - ϵ curves of the cores.

It is well known that the load-carrying capacity of BRBs under pure compression is closely related to the material constitutive relation, the element type, and the boundary conditions of BRBs. The FEM adopted to analyze the load-carrying capacity of the CAS-BRB has been validated by a hysteretic test for CS-BRBs (as shown in Figure 6), which is carried out by Zhu et al. [22] and Tong et al. [26]. Both the CS-BRB and CAS-BRB have similar material constitutive relations, element types, and boundary conditions. Therefore, the accuracy of the FEM in this article can be accepted.

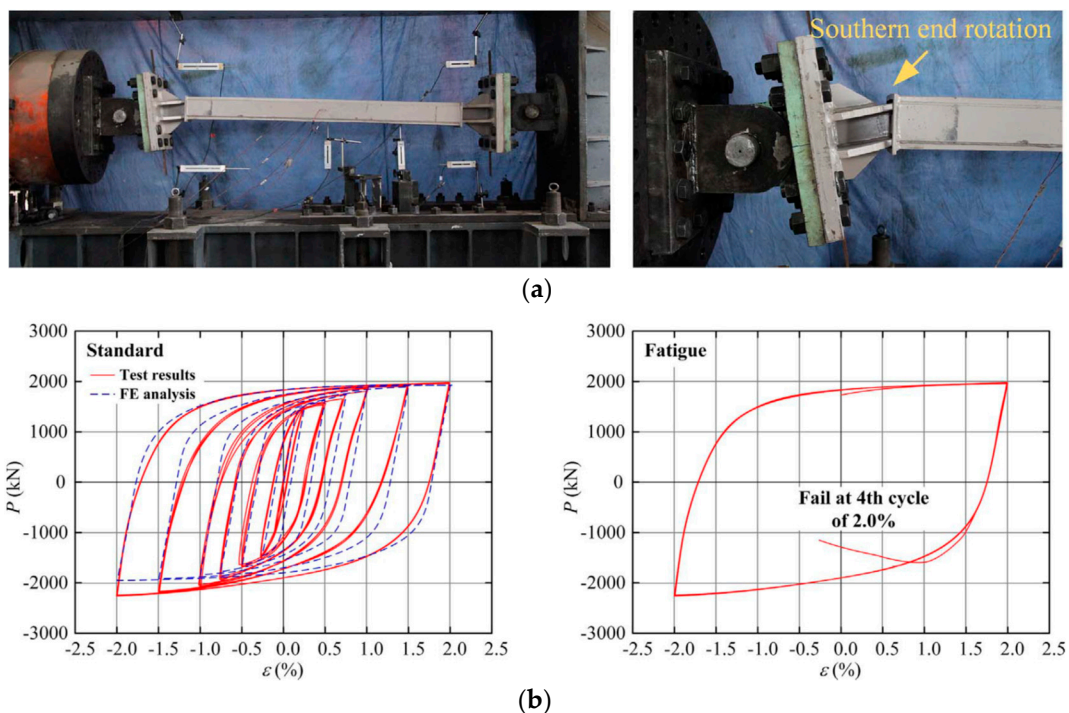


Figure 6. Verification of the FEM adopted in this study using the experimental results of Zhu et al. [22] and Tong et al. [26]. (a) Observed performance of CS-BRB specimens. (b) Hysteretic responses were obtained from tests and FE analyses.

4.2. Axial Elastic-Plastic Bearing Capacity

Based on the finite element model (FEM) of the steel tube restrained core split BRB, four sets of examples were designed based on the width-thickness ratio and the CSA-BRB length of the core, as shown in Table 1. The lateral stiffness of the restrained external system

is modified in each of these scenarios by changing the height h_w of the web in the restrained external system (the spacing between the two limbs) while the cross-section of the two limbs of the CSA-BRB remains constant. The CSA-BRB cases are numbered according to CSA – l – ζ , where CSA stands for steel tube concrete restrained kernel split BRB, l is the CSA-BRB length, and ζ is the CSA-BRB's restraint ratio and is calculated according to Equation (1).

Table 1. Key geometric dimensions of different numerical examples of the CSA-BRBs.

No.	$b_c \times t_c/\text{mm}$	$P_{y,c}/\text{kN}$	$b_f \times h_f \times t_f/\text{mm}$	t_w/mm	h_w/mm	ζ
CSA-20- ζ	240×40	4512	$400 \times 200 \times 10$	10	100~320	1.15~3.13
CSA-18- ζ	240×30	3384	$360 \times 150 \times 10$	10	100~320	1.04~3.40
CSA-15- ζ	240×24	2707	$336 \times 120 \times 8$	10	120~300	1.26~3.64
CSA-12- ζ	240×24	2707	$336 \times 120 \times 8$	10	60~200	1.17~3.32

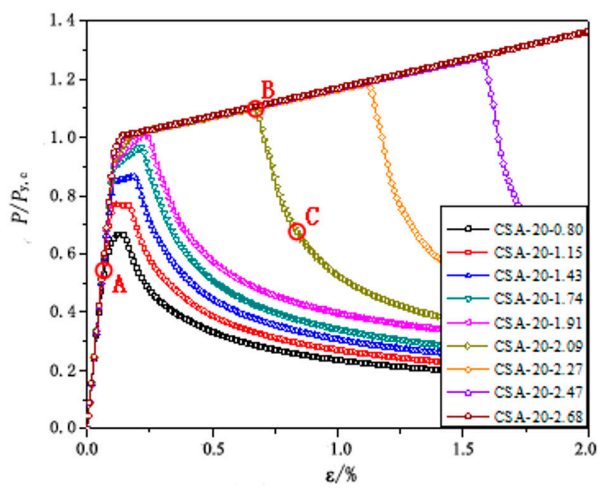
An elastic buckling analysis was carried out for the arithmetic example in Table 1, and the restraint ratio was calculated by Equation (1). On this basis, the elastoplastic bearing capacity of the monotonic axial compressive load is analyzed for the designed example, and the ultimate compressive bearing capacity of CSA-BRB under axial monotonic load is obtained. The stability factor φ of the CSA-BRB is calculated from this. In the calculation, an initial geometric defect of the first-order buckling mode is applied to the CSA-BRB, the initial flaw amplitude of which is taken to be 1/500 of the length of the member, where the residual stresses in the CSA-BRB are equivalently taken into account. The additional effect of residual stresses in the asset is equivalent. Figures 7 and 8 illustrate the load-displacement curves, the deformation, and stress distributions of a member in various stages for some instances. Following the Code for Seismic Design of Building Structures (GB50011-2016) [26], the kernel axial displacement must be added to meet the strain requirement of 0.02.

Based on the load-displacement curves given in Figure 7 and the stress and deformation diagrams shown in Figure 8, the influence of the restraint ratio on the failure mode of the CSA-BRB can be analyzed. With the help of the concept of the column stability factor, the ratio of the ultimate load of the CSA-BRB to the core yield load can be defined as the stability factor φ .

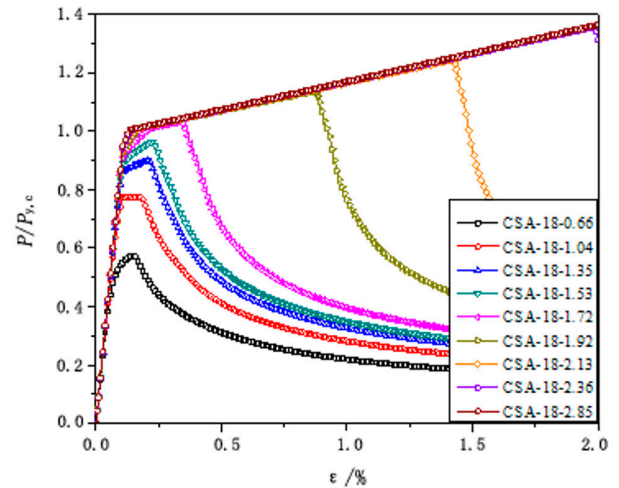
For CSA-20-0.80, the low restraint capacity of its external restraining members on the core makes its restraint ratio $\zeta < 1.0$; that is, the CSA-BRB is bound to experience overall instability before the core yields when the stability factor φ is less than 1.

Despite their restraint ratios, the CSA-20-1.15, CSA-20-1.43, and CSA-20-1.74 experience overall instability before the entire portion of the core yields, even when undesirable effects, such as initial mount faults, are taken into consideration. The stability factor $\varphi < 1.0$ declines as the restraint ratio ζ decrease when the CSA-BRB reaches its peak axial compression load at an axial compressive strain $\varepsilon = 0.001$ in the core. After the overall instability occurs, the axial load-carrying capacity of the specimen rapidly decreases, and the CSA-BRB is subsequently damaged. The maximum stress in the external restraining members has already yielded when the CSA-BRB reaches its peak load, after which the plastic zone expands rapidly, and the CSA-BRB undergoes overall instability.

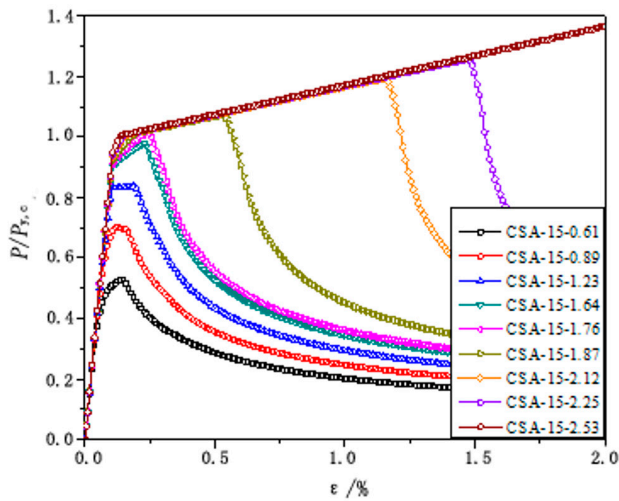
For CSA-20-1.91, CSA-20-2.09, CSA-20-2.27, and CSA-20-2.47, the restraint ratio ζ of the CSA-BRB is more significant, and when the axial compressive strain in the core is $\varepsilon = 0.001$, the core yields in the entire section and its stability coefficient $\varphi \geq 1.0$. After that, the core enters the strengthening phase, and its stability coefficient φ rises slowly with the increase in the axial compressive strain. When the axial compressive strain reaches a particular value, the overall instability of the CSA-BRB occurs, and its bearing capacity decreases rapidly. According to the FE simulation process, the external restraining members of the CSA-BRB expand in the plastic zone in the span, causing its overall instability. The stress distribution of CSA-BRB CSA-20-1.91 in the elastic phase, limit state, and final state is shown in Figure 8.



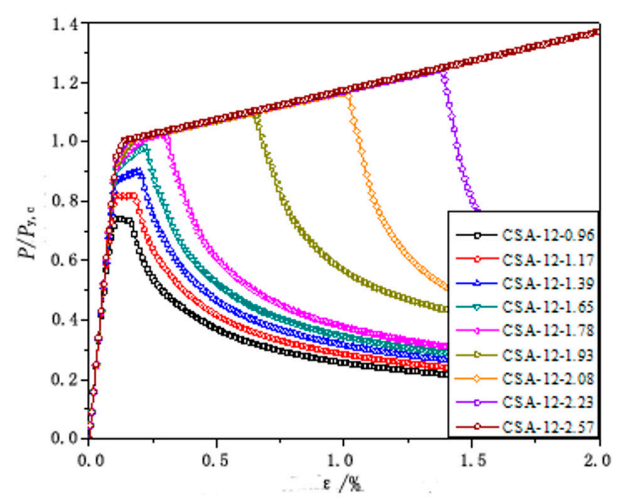
(a) CSA-20- ζ



(b) CSA-18- ζ



(c) CSA-15- ζ



(d) CSA-12- ζ

Figure 7. Axial load-displacement curves for numerical examples No. 1, 2, 3, and 4, respectively.

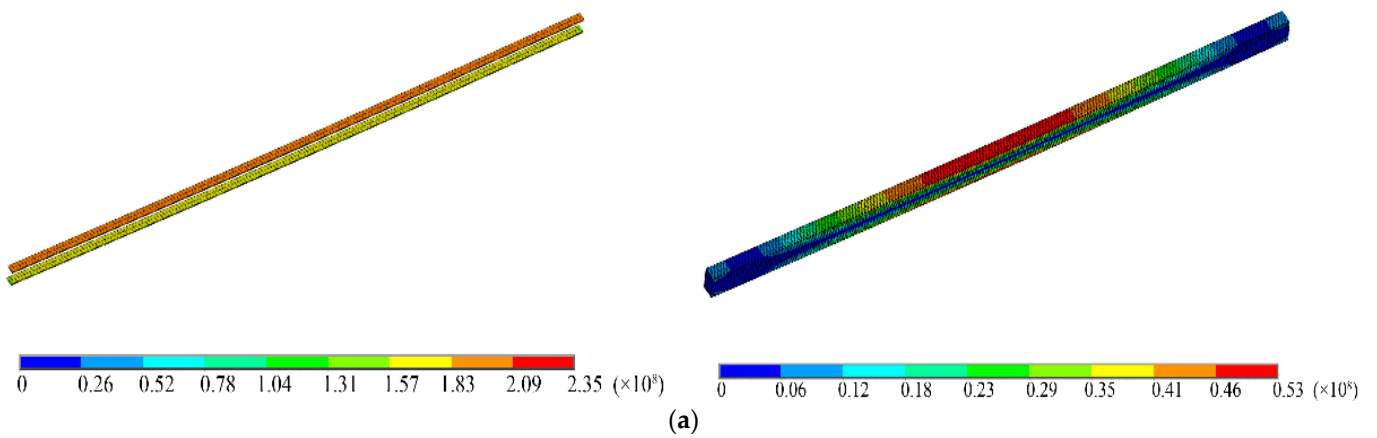


Figure 8. Cont.

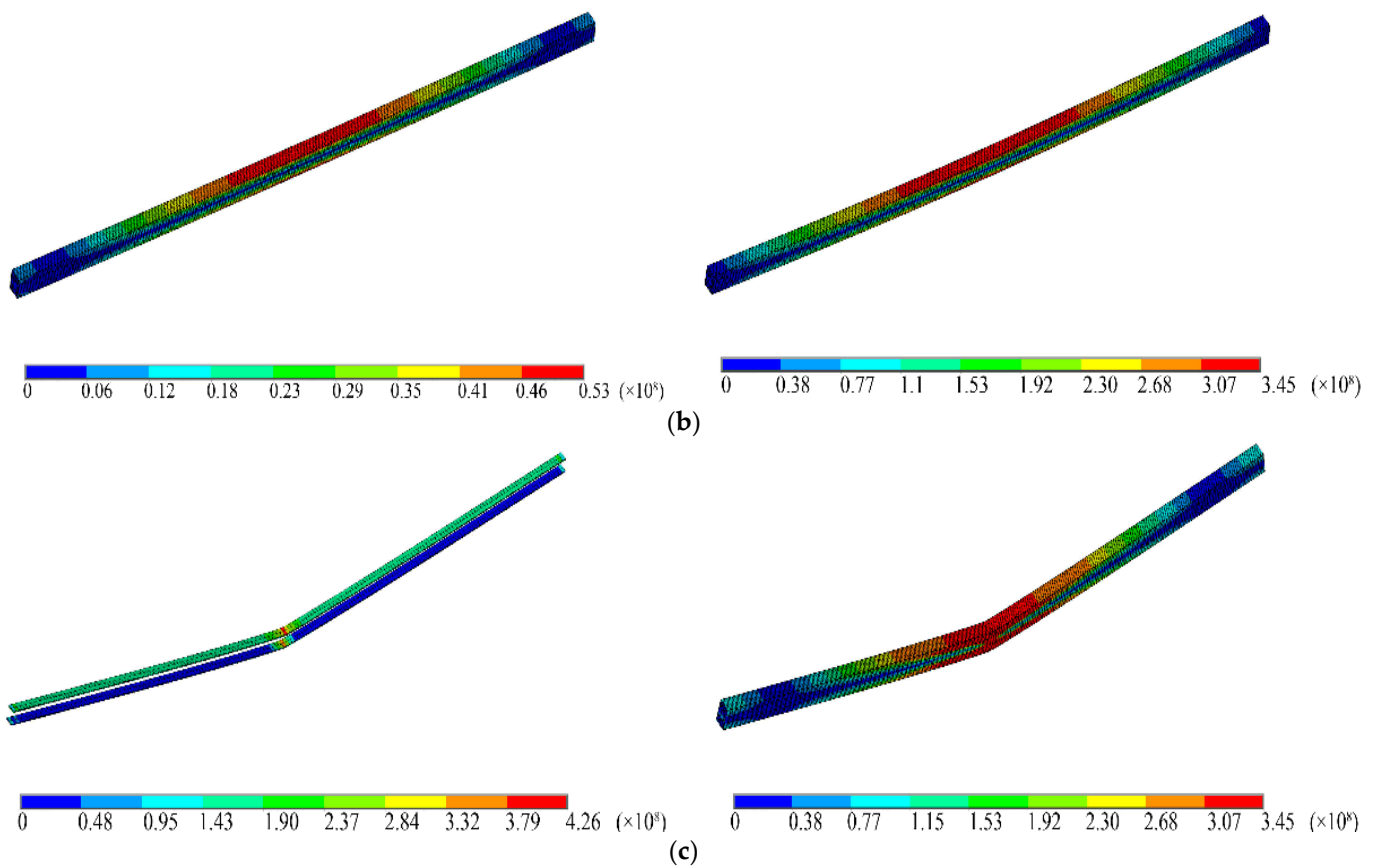


Figure 8. Stress distribution and deformation of example CSA-20-1.91 at points A, B, and C in Figure 6a. (a) von Mises stresses and lateral deformations for the initial yield state of the core of the CSA-BRB at point A in Figure 6a. (b) von Mises stresses and lateral deformations for the ultimate state of the core of the CSA-BRB at point B in Figure 6a. (c) von Mises stresses and lateral deformations for the final state of the core of the CSA-BRB at point C in Figure 6a.

For CSA-20-2.68, the constraint ζ is relatively large so that none of the CSA-BRB experience overall instability at the core strain of 0.02. From the initial yielding of the CSA-BRB core to when the strain reaches 0.02, the strengthening effect of the core material is noticeable, and the CSA-BRB core corresponds to the stability coefficient $\varphi = 1.37$ when the strain is 0.02. The results of the FE calculations show that the CSA-BRB's external restraining members remain elastic throughout the load phase. As a result, the general stability of the service is not affected.

Based on the FE analysis results, the damage mode and functional requirements of the core-separated BRB under monotonic load can be divided into three categories according to the restraint ratio: when the restraint ratio of the CSA-BRB is small, the external constraint system is not sufficient to constrain the core member to reach complete section yielding, which means that plastic deformation occurs and the CSA-BRB as a whole is destabilized and damaged, which is the first type of damage. With the expansion of the combined section of the external restraining members, the lateral stiffness of the section increases, i.e., the restraint ratio of the CSA-BRB also increases. At this time, the kernel member can reach the entire section yielding but still cannot meet the load requirement of 0.02 strain. Strengthening leads to the increase in the axial pressure of the core, the deformation of the external restraining members, and the overall instability of the CSA-BRB, which is the second type of failure. In the last case, the restraint ratio of the asset is large enough to meet the requirement that the kernel member achieves total section yield and the axial compressive strain of the CSA-BRB reaches $\varepsilon = 0.02$. The CSA-BRB does not experience overall instability.

4.3. Restraint Ratio Thresholds for Bearing Elements

Each group of cases in the critical state where the compressive strain of the core member exceeds 0.02, while the external restraining members' outermost edge fibers yield is chosen based on the results of static elastoplastic load carrying capacity calculations for the four sets of cases, as shown in Table 2, to determine its bending moment ($M_{e,FE}$) in the span under the action of the axial load $M_{e,FE}$. The correction coefficients for the four groups of calculation examples can be found by comparing them to the Equation (5) calculation results. The maximum value is $\alpha = 1.8$ conservatively taken and recommended.

Table 2. Key geometric dimensions and results of the CSA-BRBs.

No.	$P_{y,c}/kN$	P/kN	δ/m	$M_{e,FM}/kN\cdot m$	$M_{e,0}/kN\cdot m$	α
CSA-20-2.68	4512	6090	0.14	861	506	1.70
CSA-18-2.60	3384	4616	0.13	625	356	1.76
CSA-15-2.75	2707	3702	0.11	429	239	1.80
CSA-12-2.75	2707	3719	0.08	310	177	1.75

Equation (6) gives an approximate formula for the restraint ratio threshold of the bearing CSA-BRB. The material over-strengthening factor $\eta = 1.37$ is considered for the core steel reinforced after yielding, and the axial compressive strain reaches 0.02. Take the first group of calculation examples in Table 1, the calculation example CSA-20- ζ in Figure 6a as an example. For the calculation example CSA-20-2.47, the restraint ratio threshold $[\zeta]_{\eta} = 2.56$ is calculated by Equation (6), at which time its restraint ratio is less than its restraint ratio threshold. The external constraint stiffness is theoretically insufficient to cause instability damage, which is in line with the numerical analysis results, as shown in Figure 6a. As the restraint ratio increases, the restraint ratio threshold $[\zeta]_{\eta} = 2.46$ for CSA-20-2.68 is calculated by Equation (6), which is less than its restraint ratio. Therefore, this calculation case can meet the requirement of the core member reaching the entire section yielding and the axial compressive strain of the CSA-BRB reaching $\varepsilon = 0.02$, which is also consistent with the numerical analysis results, as shown in Figure 6a. The other three cases in Table 1 are similar to the first set of circumstances, and their numerical FEM results are also consistent with the results of Equation (6). Given this, the restraint ratio threshold of CSA-BRB can be determined more accurately by using Equation (6).

During the preliminary design phase of the CSA-BRB, a conservative estimate of its restraint ratio threshold is required. Therefore, the restraint ratio threshold value can be obtained by plotting the relationship between the restraint ratio ζ and the stability coefficient φ of the four groups of calculation examples in Figure 9.

When the coefficient of stability of the CSA-BRB $\varphi < 1.0$, i.e., the CSA-BRB core, has not yet reached the initial yield, it has already failed, which belongs to the first type of failure mentioned above; as the restraint ratio φ of the CSA-BRB increases, the stability coefficient increases. When the CSA-BRB's stability coefficient is within the range of $1.0 \leq \varphi < 1.37$, the CSA-BRB's kind of damage is the second type, and the restraint ratio is within the range of $1.8 \leq \zeta < 2.8$ at the same time. When the restraint ratio of the CSA-BRB $\zeta = 2.8$, the axial compressive strain of the core member $\varepsilon = 0.02$, it happens that the overall instability of the CSA-BRB does not occur, so the restraint ratio threshold value of the CSA-BRB is approximately taken as $[\zeta]_{\eta} = 2.8$, so when the restraint ratio of the CSA-BRB $\zeta \geq 2.8$, it can be considered that the CSA-BRB meets the requirements of the bearing type. It has a certain plastic deformation and strengthening capacity.

The references [21,22] give the restraint ratio threshold value of 1.8 and 2.0 for CS-BRB bearing members with solid web and wave web connections, respectively, where the restraint ratio threshold value for bearing members is defined as the core member reaching the entire section initial yielding and the CSA-BRB undergoing integral instability damage. At that point, the corresponding stability factor $\varphi = 1.0$. Although this type of member can provide bearing capacity, the axial compressive strain of the core member does not meet

$\varepsilon \geq 0.02$, and it cannot plastically deform and strengthen. When the stability coefficient of CSA-BRB is $\varphi = 1.0$, the restraint ratio threshold value is 1.8, which is also consistent with the calculation results of reference [22], which shows that the FE calculation results in this paper are accurate.

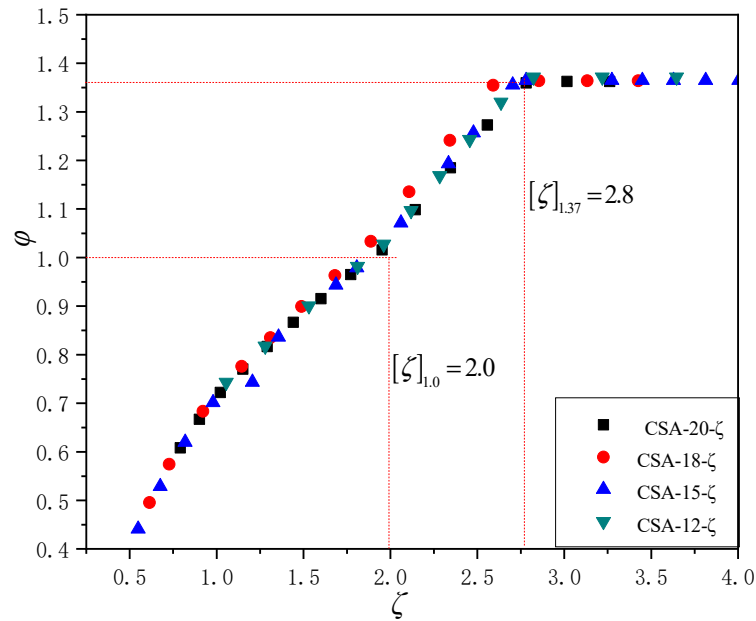


Figure 9. φ - ζ of the CSA-BRBs in Table 2.

5. Hysteretic Energy Dissipation Performance

5.1. Material Ontology Modeling

Unlike monotonic load, the reciprocal load of a core member under axial reciprocal load results in a significant increase in material strengthening, so the ideal elastoplastic instanton (bilinear model) relationship is no longer applicable to hysteretic load simulations. In the FE analysis, the bilinear isotropic strengthening model BISO in the ANSYS14.5 software; the strengthening model CHAB considers the non-linear effect between strengthening and plasticity and is suitable for considerable strain and cyclic load. As a result, a combination of the non-linear random strengthening CHAB model and the bilinear isotropic strengthening BISO model provided by ANSYS was used in the FE simulation of the hysteresis performance of the steel tube constrained core separated BRB, which can reasonably simulate the steel’s hysteresis performance when the steel material’s BISO model is not set to strengthen the segment, as illustrated in Figure 10.

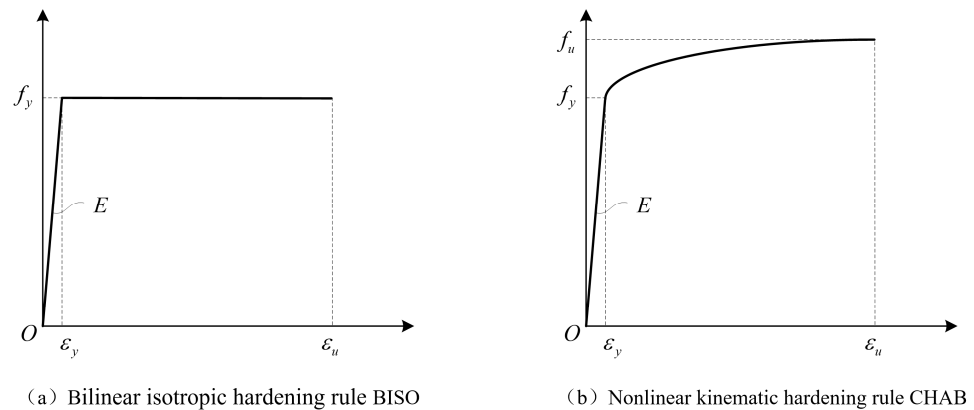


Figure 10. The material constitutive relationships for steel components in the FE models of CSA-BRBs.

The non-linear follow-through strengthening CHAB model is a material ontological model proposed by Chaboche based on the elastic-plastic stability theory that uses the steel hysteresis skeleton curve to establish a cyclic ontological model of steel for hysteresis simulation. In this section, based on the CHAB model provided by this theory, four kinds of follow-up reinforcement models are superimposed (Figure 10b). The parameters C and γ in the model are selected from these data provided in the reference [27] $C_1 = 6.0$ GPa and $\gamma_1 = 173$, $C_2 = 5.0$ GPa and $\gamma_2 = 120$, $C_3 = 3.0$ GPa and $\gamma_3 = 32$, $C_4 = 9.9$ GPa and $\gamma_4 = 35$, respectively.

5.2. Hysteretic Load System

According to the Code for Seismic Design of Buildings (GB50011-2016) [28], the inter-story angle of frame structures under large-scale earthquakes should not be greater than $1/50$. When the BRB is arranged obliquely, the axial strain in the core is approximately 0.02. Therefore, the maximum axial displacement of the core is taken as $2\%l_y$ in the analysis of the steel tube restrained core separated BRB elastic-plastic hysteresis. According to the recommendation of AISC341-05 in the United States, the displacement load amplitude is taken from small to large as six grades of $0.25\%l_y$, $0.50\%l_y$, $0.75\%l_y$, $1.00\%l_y$, $1.50\%l_y$ and $2.00\%l_y$, and three tension-compression cycles are performed at each level of displacement load amplitude. The load regime of the CSA-BRB under repeated loads is shown in Figure 11.

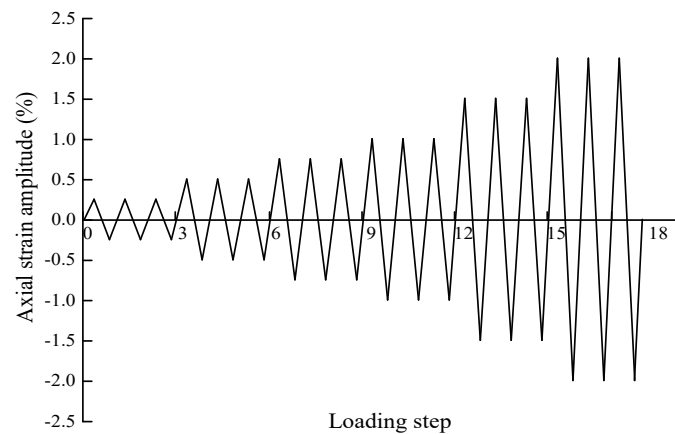


Figure 11. Hysteretic load protocol of CSA-BRBs.

5.3. Hysteretic Energy Dissipation Performance

Based on the numerical results of the static bearing capacity of the CSA-BRB, an example of the stability coefficient $\varphi \geq 1.0$ is selected to analyze the elastic-plastic hysteretic performance, as shown in Table 3. The height of the web h_w (i.e., the spacing between the two limbs) in the external restraining members was varied to change the lateral stiffness of the external restraining members. In comparison, the cross-section and length of the two limbs of the CSA-BRB remain unchanged. Similarly, the CSA-BRB case is numbered according to the following formula $CSA - l - \zeta$, where CSA stands for steel tube concrete restrained kernel split BRB, l is the length of the CSA-BRB, and ζ is the restraint ratio of the CSA-BRB.

Table 3. Key geometric dimensions and results of the various components of CSA-BRB.

No.	$b_c \times t_c/mm$	$P_{y,c}/kN$	$b_f \times h_f \times t_w/mm$	h_w/mm	ζ	φ
CSA-20- ζ	240 × 40	4512	400 × 200 × 10	200~340	1.91~3.37	1.03~1.60
CSA-18- ζ	240 × 30	3384	360 × 150 × 10	180~340	1.72~3.70	1.00~1.60
CSA-15- ζ	240 × 24	2707	336 × 120 × 8	180~310	1.87~3.82	1.02~1.60
CSA-12- ζ	240 × 24	2707	336 × 120 × 8	110~220	1.78~3.74	1.00~1.60

Based on the results of the calculations, the CSA-BRB is divided into three types of modes based on its hysteretic energy consumption performance, as illustrated by the CSA-20- ζ group calculation.

Firstly, in axial load reciprocating load, the CSA-BRB core has not reached the total cross-section yield, i.e., the stability coefficient φ is less than 1.0, which cannot fully load an entire hysteretic loop during the hysteretic load process. The hysteresis curve of this type of CSA-BRB is severely pinched, and the energy dissipation capacity is low, so it cannot be used as an energy dissipation CSA-BRB for the seismic design of the structure.

Secondly, when the stability coefficient of the CSA-BRB is within the range of $1.0 \leq \varphi < 1.6$, in the axial load reciprocal load process, the core reaches complete cross-sectional yielding and enters the strengthening phase. This type of CSA-BRB completes the low-order hysteresis load, and only part of the hysteresis curve is full. Still, it cannot satisfy the established load requirements of energy dissipation capacity. Although this type of CSA-BRB has a particular energy dissipation performance, it cannot meet the plastic cumulative strain value requirements. There is no problem with the use of bearing members. It can be used to adjust the lateral stiffness of the structure, but it cannot be used for the energy dissipation design of the system.

Thirdly, the type of CSA-BRB can be used as a dissipating energy member because it can fulfill the plastic cumulative strain value requirements, and the hysteresis curve is complete when the coefficient of stability of the CSA-BRB is 1.6.

Take the calculation example CSA-20-2.90 (Figure 12) in the first group of calculation examples in Table 3 as an example; its restraint ratio is $\zeta = 2.90$. During the monotonic load process, when the axial compressive strain of the core in this example reaches 0.02, the CSA-BRB does not have an overall instability failure. Nevertheless, in the hysteretic analysis of the reciprocating axial load, when the axial strain of the core reaches 0.015, the overall instability and loss of the CSA-BRB occurred, which failed to meet the requirements of the energy-dissipating CSA-BRB for the cumulative plastic deformation index of the core, and did not form a complete hysteresis curve. The comparison of the calculation results of monotonic and reciprocating load shows that the axial strain requirements for the core member are both 0.02. Still, the energy-dissipating CSA-BRB has a more stringent requirement for cumulative plastic deformation than the bearing CSA-BRB and a higher requirement for the restraint ratio. It can be seen from Figure 12h that when the cumulative plastic strain reaches 0.02, the strengthening stress of its core material has become 1.6 times the initial yield stress, which is the coefficient $\omega = 1.6$ in Equation (8).

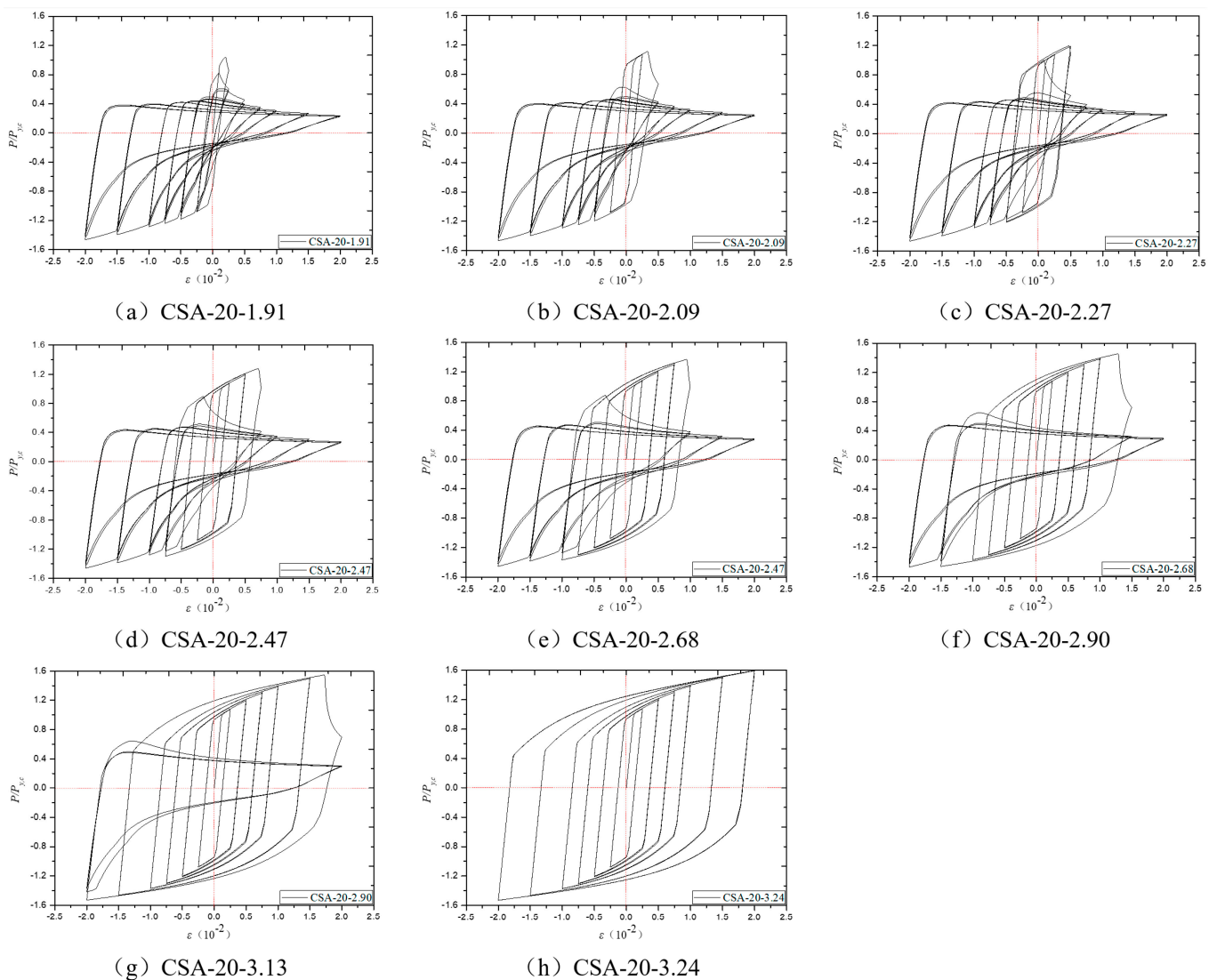


Figure 12. Hysteretic curves for numerical examples (No. 1) in Table 3.

5.4. Restraint Ratio Threshold of CSA-BRB Energy-Dissipating Type

Equation (7) proposed the formula for the restraint ratio threshold of the energy-dissipating CSA-BRB $\omega = 1.6$. The first set of examples in Table 3, i.e., group CSA-20- ζ in Figure 11, is used. For the example, CSA-20-3.13, the restraint ratio threshold $[\zeta]_{\omega} = 3.14$ is calculated by Equation (7). Since the restraint ratio is less than the restraint ratio threshold, the components cannot complete the entire hysteresis load process, and the hysteresis curve is not total. It does not meet the requirements of energy-dissipating members, which is consistent with the numerical analysis results, as shown in Figure 12g. With the increase in the restraint ratio, the example CSA-20-3.24 is selected, and its restraint ratio threshold $[\zeta]_{\omega} = 2.97$ is calculated by Equation (7), which is smaller than its restraint ratio. Therefore, this example can complete the hysteretic load process. The curves are plump and meet the requirements of energy-dissipating type, consistent with the numerical analysis results, as shown in Figure 11h. For the other three sets of cases in Table 3, the FE calculation results are consistent with Equation (7). As a result, using Equation (7), the restraint ratio threshold of CSA-BRB may be computed more precisely. Table 4 shows the results of the FE hysteresis energy consumption calculations for the four sets of instances, along with a measure of how full their hysteresis curves are.

Table 4. Results of hysteretic load protocol of CSA-BRB specimens.

No.	h_w	ζ	φ	Hysteretic Curve
CSA-20- ζ	200~330	1.91~3.24	1.03~1.60	pinch
	330~340	3.24~3.36	1.60	plump
CSA-18- ζ	180~300	1.72~3.12	1.00~1.60	pinch
	300~340	3.12~3.70	1.60	plump
CSA-15- ζ	180~280	1.87~3.30	1.02~1.60	pinch
	280~310	3.30~3.82	1.60	plump
CSA-12- ζ	110~200	1.78~3.30	1.00~1.60	pinch
	200~220	3.30~3.74	1.60	plump

Similarly, in the preliminary design stage of CSA-BRB, it is necessary to estimate the restraint ratio threshold value conservatively. As a result, Figure 13 depicts the link between the restraint ratio ζ and stability factor φ for each of the four sets of calculations. The restraint ratio threshold value can be obtained. As shown in Figure 13, when the restraint ratio of the CSA-BRB ($\zeta \geq 3.30$), the CSA-BRB can meet the requirement of hysteretic performance for energy-dissipating members without damage, and the hysteretic curve is whole, satisfying the requirement of the cumulative plastic deformation capacity factor ($\mu_c \geq 200$) in AISC341-05. Therefore, $\zeta \geq 3.30$ it can be used as the restraint ratio threshold value for energy-dissipating bracing for its preliminary design.

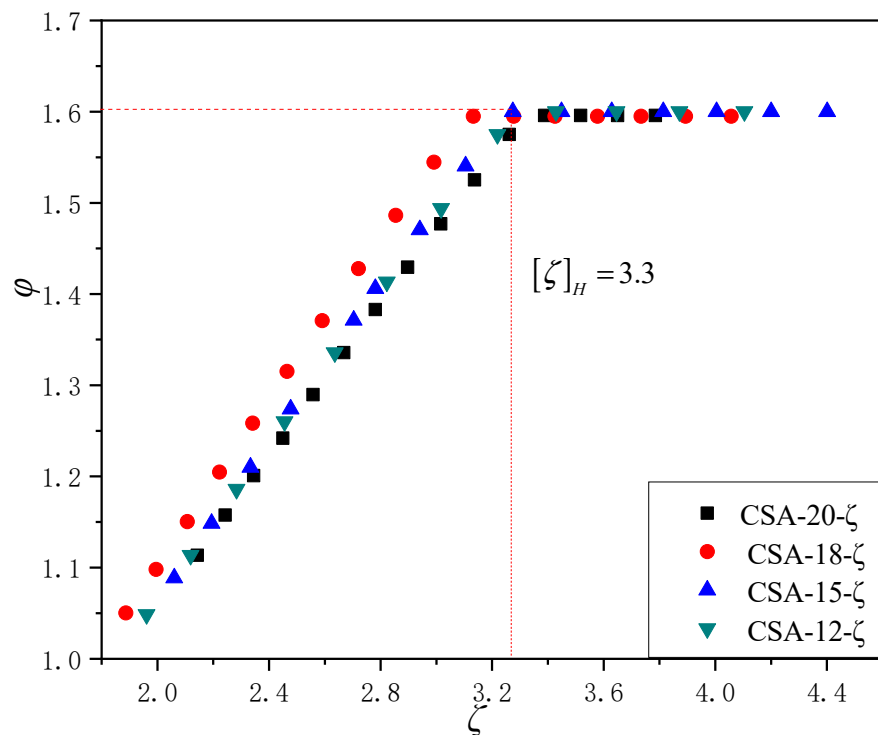


Figure 13. φ -of the CSA-BRBs in Table 1 under cyclic axial loads.

6. Conclusions

This paper mainly studies the bearing capacity and hysteretic energy dissipation performance of the CSA-BRB with the separated core. (1) The maximum value of the bending moment in the CSA-BRB span corresponding to the core achieving a compressive strain of 0.02 is not greater than the flexural bearing capacity of the outermost edge of the external restraining members when it yields an approximate calculation equation for the restraint ratio threshold $[\zeta]_\eta$ for bearing members, and the restraint ratio threshold $[\zeta]_\omega$ for energy-dissipating members were developed, respectively. The accuracy of the calculation

equation was assessed. (2) The CSA-BRB simplified computation model and accompanying FEM have been constructed. The elastic-plastic bearing capacity under monotonic axial compression load was investigated using a variety of calculation situations. The relationship curve between the ultimate bearing capacity of the CSA-BRB and the restraint ratio is drawn based on the calculation results of the above cases, the requirement that the axial strain of the core reaches 0.02, and the restraint ratio threshold of the bearing member is regarded as $[\zeta]_y = 2.8$. (3) Based on the results of the hysteretic energy dissipation FE analysis of the CSA-BRB under axial reciprocating load, the threshold value of the energy dissipative CSA-BRB restraint ratio threshold is given as $[\zeta]_{\omega} = 3.3$ based on whether the cumulative plastic deformation capacity factor ($\mu_c \geq 200$) in AISC341-05 can be satisfied.

Author Contributions: Conceptualization, B.Z.; Methodology, B.Z.; Validation, J.Z.; Formal analysis, Y.Y.; Investigation, J.Z.; Data curation, Y.Y. All authors have read and agreed to the published version of the manuscript.

Funding: This research was funded by the Fundamental Research Funds for the Central Universities (No. FRF-TP-20-033A1).

Institutional Review Board Statement: Not applicable.

Informed Consent Statement: Not applicable.

Data Availability Statement: The data presented in this study are available on request from the corresponding author.

Conflicts of Interest: The authors declare no conflict of interest.

References

1. Liu, J. *Research on the Design Theory of Buckling-Restrained Braces and Buckling-Restrained Braces Frames*; Tsinghua University: Beijing, China, 2005.
2. Guo, Y.; Zhang, B.; Wang, X. Research progress on design theory of assembled buckling-restrained brace. *J. Archit. Civ. Eng.* **2013**, *30*, 1–12.
3. Nagao, T.; Mikuriya, K.; Matsumoto, Y. An experimental study on the elasto-plastic behavior of unbonded composite bracing (part 1–4). In *Summaries of Technical Papers of Annual Meeting of the Architectural Institute of Japan*; Structural Engineering Section II: Tokyo, Japan, 1988; pp. 1329–1336.
4. Inoue, K.; Sawaisumi, S. Bracing design criterion of the reinforced concrete panel including unbonded steel diagonal braces. *J. Struct. Constr. Eng.* **1992**, *432*, 41–49.
5. Kimura, K.; Yoshioka, K.; Takeda, T.; Fukuya, Z.; Takemoto, K. Tests on braces encased by mortar in-filled steel tubes. In *Summaries of Technical Papers of Annual Meeting*; Architectural Institute of Japan: Tokyo, Japan, 1976; pp. 1041–1042.
6. Guo, Y.; Jiang, L. Behavior and application of buckling-restrained braces assembled with section steels. *Build. Struct.* **2010**, *40*, 30–37.
7. Zhao, J.X.; Wu, B.; Ou, J.P. A novel type of angle steel buckling-restrained brace: Cyclic behavior and failure mechanism. *Earthq. Eng. Struct. Dyn.* **2011**, *40*, 1083–1102. [[CrossRef](#)]
8. Zhao, J.; Wu, B.; Li, W.; Qu, J. Local buckling behavior of steel angle core in buckling-restrained braces: Cyclic tests, theoretical analysis, and design recommendation. *Eng. Struct.* **2014**, *66*, 129–145. [[CrossRef](#)]
9. Hoveidae, N.; Tremblay, R.; Rafezy, B.; Davaran, A. Numerical investigation of seismic behavior of short-core all-steel buckling restrained braces. *J. Constr. Steel Res.* **2015**, *114*, 89–99. [[CrossRef](#)]
10. Judd, J.P.; Marinovic, I.; Eatherton, M.R.; Hyder, C.; Phillips, A.R.; Tola, A.T.; Charney, F.A. Cyclic tests of all-steel web-restrained buckling-restrained brace subassemblages. *J. Constr. Steel Res.* **2016**, *125*, 164–172. [[CrossRef](#)]
11. Guo, Y.L.; Zhou, P.; Wang, M.Z.; Pi, Y.L.; Bradford, M.A. Numerical studies of cyclic behavior and design suggestions on triple-truss-confined buckling-restrained braces. *Eng. Struct.* **2017**, *146*, 1–17. [[CrossRef](#)]
12. Guo, Y.-L.; Zhu, J.-S.; Zhou, P.; Zhu, B.-L. A new shuttle-shaped buckling-restrained brace. *Theoretical study on buckling behavior and load resistance. Eng. Struct.* **2017**, *147*, 223–241.
13. Guo, Y.-L.; Zhou, P.; Wang, M.-Z.; Pi, Y.-L.; Bradford, M.A.; Tong, J.-Z. Experimental and numerical studies of hysteretic response of triple-truss-confined buckling-restrained braces. *Eng. Struct.* **2017**, *148*, 157–174. [[CrossRef](#)]
14. Jia, L.J.; Ge, H.; Maruyama, R.; Shinohara, K. Development of a novel high performance all-steel fish-bone shaped buckling-restrained brace. *Eng. Struct.* **2017**, *138*, 105–119. [[CrossRef](#)]
15. Tong, J.Z.; Guo, Y.L. Numerical investigations on elastic buckling and hysteretic behavior of steel angles assembled buckling-restrained braces. *J. Constr. Steel Res.* **2018**, *144*, 21–39. [[CrossRef](#)]

16. Qu, B.; Liu, X.; Hou, H.; Qiu, C.; Hu, D. Testing of Buckling-Restrained Braces with Replaceable Steel Angle Fuses. *J. Struct. Eng.* **2018**, *144*, 04018001. [[CrossRef](#)]
17. Sun, J.; Pan, P.; Wang, H. Development and experimental validation of an assembled steel double-stage yield buckling restrained brace. *J. Constr. Steel Res.* **2018**, *145*, 330–340. [[CrossRef](#)]
18. Wang, C.-L.; Gao, Y.; Cheng, X.; Zeng, B.; Zhao, S. Experimental investigation on H-section buckling-restrained braces with partially restrained flange. *Eng. Struct.* **2019**, *199*, 109584. [[CrossRef](#)]
19. Jiang, T.; Dai, J.; Yang, Y.; Liu, Y.; Bai, W. Study of a new-type of steel buckling-restrained brace. *Earthq. Eng. Eng. Vib.* **2020**, *19*, 239–256. [[CrossRef](#)]
20. Guo, Y.L.; Zhang, B.H.; Jiang, Z.Q.; Chen, H. Critical load and application of core-separated buckling-restrained braces. *J. Constr. Steel Res.* **2015**, *106*, 1–10. [[CrossRef](#)]
21. Guo, Y.; Zhang, B.; Zhu, B. Restrain ratio of all-steel core-separated buckling-restrained braces. *J. Build. Struct.* **2015**, *36*, 133–141.
22. Zhu, B.-L.; Guo, Y.-L.; Zhou, P.; Bradford, M.A.; Pi, Y.-L. Numerical and Experimental Study of Corrugated-Web-Connected Buckling-Restrained Braces. *Eng. Struct.* **2017**, *134*, 107–124. [[CrossRef](#)]
23. Huang, F.; Duan, H.; Cheng, B.; Teng, N. Hysteretic performance of all-steel assembled double-cores buckling-restrained braces using Q195 low-yield core. *J. Constr. Steel Res.* **2021**, *187*, 106925. [[CrossRef](#)]
24. Fang, S. *Study in Preparation of Ceramisite Cellular Concrete and Its Basic Performance*; North China University of Technology: Beijing, China, 2014.
25. *AISC 341-05*; Seismic Provisions for Structural Steel Buildings. American Institute of Steel Construction: Chicago, IL, USA, 2005.
26. Guo, Y.-L.; Tong, J.-Z.; Zhang, B.-H.; Zhu, B.-L.; Pi, Y.-L. Theoretical and experimental investigation of core-separated buckling-restrained braces. *J. Constr. Steel Res.* **2017**, *135*, 137–149. [[CrossRef](#)]
27. Shi, Y.; Wang, M.; Wang, Y. Experimental and constitutive model study of structural steel under cyclic loading. *J. Constr. Steel Res.* **2011**, *67*, 1185–1197. [[CrossRef](#)]
28. *GB 50011-2016*; Code for Seismic Design of Buildings. China Architecture & Building Press: Beijing, China, 2016.

Disclaimer/Publisher’s Note: The statements, opinions and data contained in all publications are solely those of the individual author(s) and contributor(s) and not of MDPI and/or the editor(s). MDPI and/or the editor(s) disclaim responsibility for any injury to people or property resulting from any ideas, methods, instructions or products referred to in the content.